SIMULATION AND EXPERIMENTAL VERIFICATION OF CRYSTALLINE POLYMER AND DIRECT METAL SELECTIVE LASER SINTERING

T. H. C. Childs, C. Hauser, C. M. Taylor and A. E. Tontowi

School of Mechanical Engineering, University of Leeds, LS2 9JT, UK

Abstract

A previously developed two-dimensional finite element simulation of the SLS of amorphous polymers has been extended to the study of crystalline polymers and metals. For crystalline polymers, three developments have been needed: the treatment of latent heat of melting, the modifying of a viscous densification law to allow for the crystalline fraction of material during melting and, to obtain agreement with experiments, a consideration of the absorption depth of CO_2 laser radiation into the powder bed; but the two-dimensional treatment remains sufficient. For metals, a different densification law and three-dimensional modelling have been needed for agreement with experiments on stainless steel powder beds.

Introduction

There have been several thermally-based finite element models of the Selective Laser Sintering (SLS) process: one-dimensional (1-D) [1,2], two-dimensional (2-D) [3] and three dimensional (3-D) [4]; but they have all treated only amorphous polymer SLS. This paper extends the approach in [3] to treat SLS of crystalline polymers and metals. For some purposes, two dimensional modelling is sufficient for polymers but for metals three dimensional modelling is necessary. This paper briefly reviews the structure of the simulation described in [3] and then concentrates on its development: to three dimensions; to introduce latent heat into the thermal modelling; to develop liquid-phase sintering laws for crystalline polymers and metals; and to account for laser radiation penetration to a finite depth below the powder bed surface. Simulation density and linear accuracy results are compared with experiments on nylon-12 (the commercial powder Duraform supplied by DTM) and an austenitic stainless steel powder.

Theory

Common structure of simulations. Figure 1 gives a view of the structure of all the simulations, based on [3]. Parts a and b summarise the physical idealisations. Part a shows in plan the outline of a layer, in this case rectangular, being sintered in the surface of a powder bed. The laser spot, power P, diameter d, scans in the ± x-direction with a speed U, scan length w and scan spacing s. In some cases the thermal diffusion in the time for one scan to be completed is negligible. Then, for temperature calculation in the bed, the actual scanning pattern can be replaced by scanning of a blade source in the y-direction, with width d and velocity $V = U(s/w)$: to calculate temperature away from the x-edges of the section, two-dimensional analysis is acceptable.

Part b shows shrinkage resulting from densification of a first layer (above) and a second layer (below). In 2-D analysis, the horizontal axis is the y-direction; in 3-D analysis, following a

single track, it is the x-direction: in the first case, the average laser power q per unit area is P/(wd) and in the second it is $4P/(\pi d^2)$. The simulation assumes that displacements occur as a result of densification only in the z-direction: it takes no account of surface tension or thermal expansion and so is not concerned with residual stress or distortion issues. For a first layer, the depth of sintering Δh_1 depends on the depth to which a sufficient temperature penetrates; the resulting shrunk layer thickness dh_1 is determined by mass conservation. For the second layer, powder is spread over the first layer to a depth Δh_2, greater than the machine-controlled layer thickness t_{layer}, and shrinks to dh_2. This process is repeated layer by layer. The simulation calculates the density change in each layer, from the computed temperature-time history in the powder and a sintering law, and applies mass conservation to determine the resulting shrinkage.

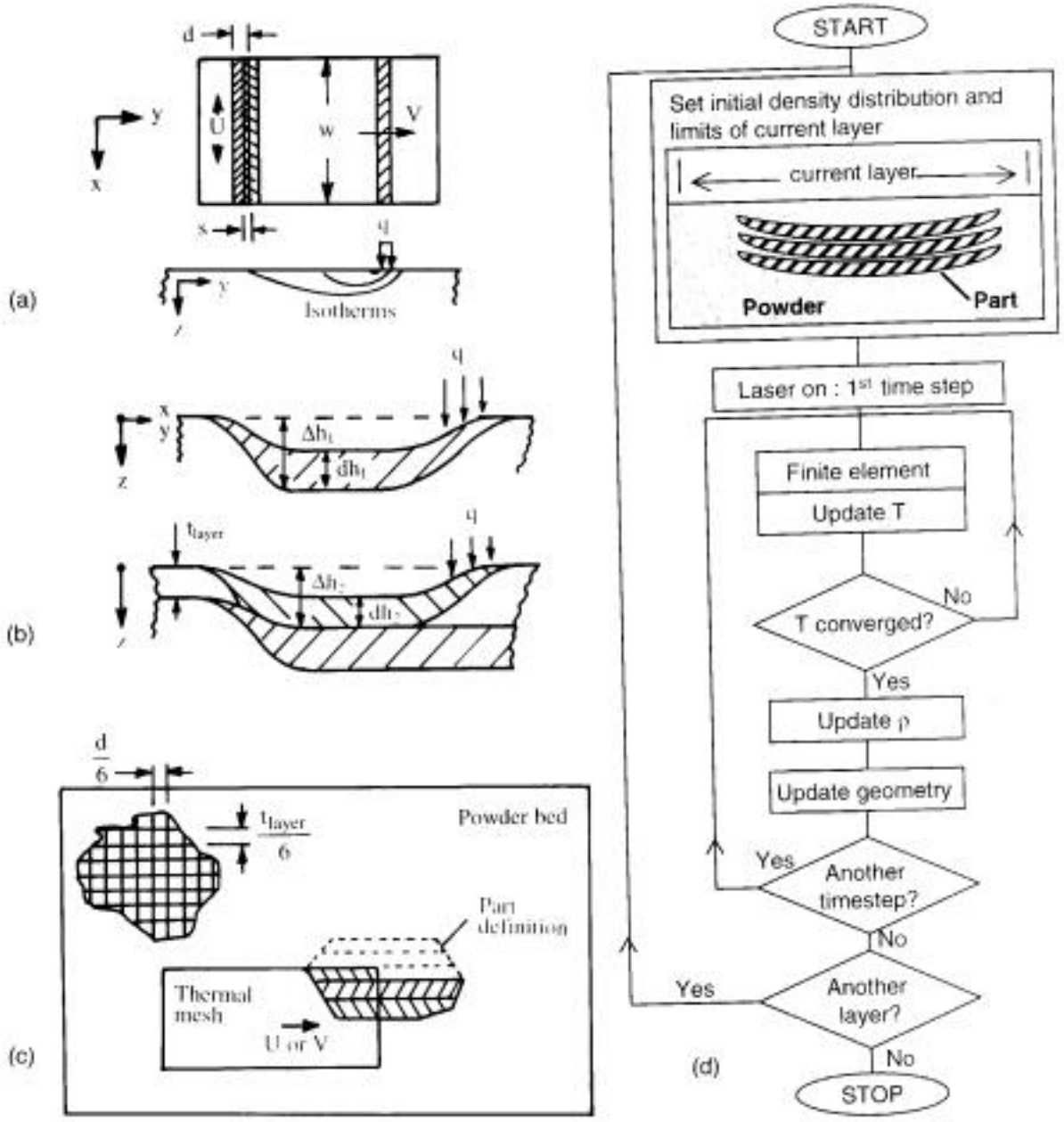

Figure 1. Prior modelling: (a,b) physical processes, (c) superposition of meshes, (d) flow chart.

The boundaries of the temperature calculation are not those of the whole powder bed, but of a finite area (2-D) or volume (3-D) round the laser blade or spot. Figure 1(c) shows, in 2-D, the superposition of the thermal finite element mesh on the powder bed. The powder bed is regarded by the calculation as a pixelated database, containing data of the variations of density and displacement in the bed. The thermal mesh moves over the bed, with the laser heat source. At the beginning of a time step, at time t, it takes the current state of the bed from the data base, operates on it over the time step Δt and returns the up-dated state to the database at time $t+\Delta t$. The thermal mesh is made up of three node triangles (2-D) or four node quadrilaterals (3-D).

Finally, Figure 1d outlines the flow chart of the calculation method. It shows, at the top, the situation in which three layers (2-D) or tracks (3-D) have already been sintered, and a fourth is about to be started. The laser is turned on and the first time step started. The first operation is a finite element non-steady-state temperature calculation over the time interval Δt. It is non-linear, both because of the densification that occurs (changing the thermal conductivity of the bed) and the variation of conductivity and specific heat with temperature (see next paragraph). There are therefore iterations until the temperature field converges. For crystalline materials, latent heat is ignored in the temperature calculation: a subsequent adjustment is made to allow for this, by the temperature recovery method [5] (see paragraph after next). Density changes are then calculated, according to an appropriate sintering law. The shrinkage geometry is then updated. The programme goes through the cycle again, until the track or layer or stack of layers is finished.

Material thermal conductivity and specific heat variations. From our experiments, the thermal conductivity of a polymer varies linearly with its porosity ε, but that of a metal does not: we have chosen an equation of the form of 1a to represent a polymer's thermal conductivity K (with K_s being the conductivity of solid material); and following [6], equation 1b to represent metal:

$$K = K_S(1 - a_K\varepsilon) \tag{1a}$$

$$K = K_s(1-\varepsilon)/\left(1 + a_K\varepsilon^{0.78}\right) \tag{1b}$$

K_S and specific heat C_p have been assumed either constant or to vary linearly with temperature:

$$K_s = K_{s,o} + a_{K,S}T \qquad C_p = C_{p,o} + a_c T \tag{2}$$

Temperature recovery method. The time-stepping finite element temperature calculation supposes that latent heat, L, is not absorbed or evolved on melting or solidifying. A sub-routine that follows it assesses whether an element is in, or has passed through, a melting or solidifying condition in the time step and adjusts the temperature (and the solid fraction) for latent heat, assuming that in one time step the heat diffusion distance is much less than the element size [5]: it has been checked that this is so. The method takes different forms depending whether melting is assumed to occur at a single temperature T_m or over a range from the solidus T_s to the liquidus T_l temperature. Here, the polymer is assumed to melt at T_m and the metal over a range T_s to T_l.

Sintering law for crystalline polymers. It has been written that crystalline polymers do not sinter by viscous flow, and therefore require a different approach to modelling their sintering rates than do amorphous polymers [2]. However, once a crystalline polymer has melted, it becomes amorphous: we propose, following studies [7] of the viscosity of crystalline polymers as they melt or solidify, with a changing crystalline fraction X, that the coefficient k' in the sintering rate equation $d\varepsilon/dt = -k'\varepsilon$, with t = time and ε = porosity, should take the form

$$k' = A_s \exp\left[-E_s/(RT)\right]\exp\left[-\beta X\right] \equiv A_s \exp\left[-\left(E_s/(RT) + \beta X\right)\right] \tag{3}$$

The first part, $A_s \exp[-E_s/(RT)]$, represents the viscous sintering of the melt, while $\exp[-\beta X]$ gives its retardation as the crystalline fraction increases. In this work, β has been empirically chosen to give agreement with the experiments reported. Values for A_s and E_s/R have been obtained as follows. The assumption has been made, following [8], that, when X = 0, k' is proportional to $\sigma/(\eta r)$: σ is melt surface tension, η is melt viscosity and r is the radius of the original powder particles. In that case, supposing that σ and η are thermally activated in an Arrhenius manner, as is the sintering rate, but noting that σ and η reduce as temperature rises (while sintering rate increases), the constant of the next equation should be the same for all polymer melt sinterings:

$$r\left[A_s \exp\left(-\frac{E_s}{RT}\right)\right]\Big/\left[A_\eta \exp\left(+\frac{E_\eta}{RT}\right)\right]\Big/\left[A_\sigma \exp\left(+\frac{E_\sigma}{RT}\right)\right] = \text{constant} \qquad (4)$$

In this work, the constant is determined from published data for a polycarbonate powder: sintering rate, size and viscosity data from [9] and surface tension data from [10]. The sintering rate constants A_s and E_s/R have then been estimated for the experimentally studied material, from equation (4), after measuring its viscosity dependence on temperature, taking its size from the supplier's data sheet and surface tension also from [10].

Sintering law for metals. Our liquid phase sintering law for metals is entirely speculative. Based on viscosity dependence on solid fraction in mushy state forming [11], we suppose there is no densification if the solid fraction X is >> 0.5; and as X reduces below 0.5, the densification is instantaneous and irreversible, to a value dependent on X. An empirical equation with these characteristics is, with the porosity ε a function of X and ε_{powder} the porosity of the powder bed,

$$1-\left(\varepsilon/\varepsilon_{powder}\right)=\left[\tanh\left(a_m[1-X]\right)\right]^n \qquad (5)$$

We have chosen $a_m = 5$ and n = 4: these values give significant densification for X < 0.7. We have also supposed that X changes from 1 to 0, linearly with temperature as temperature changes from the solidus to the liquidus temperature of the metal alloy being studied.

Absorption of laser radiation. We have found that agreement between simulation and experiments requires an assumption that the laser energy penetrates and is absorbed to a finite depth below the surface of the powder bed. We suppose the penetration depth Δz_p to vary with porosity, from zero when porosity = 0, to infinity when porosity = 1. A function of this form is

$$\Delta z_p = a_p \varepsilon/(1-\varepsilon) \qquad (6)$$

where a_p may be adjusted to give a range of depths. The program estimates energy absorption per depth as the inverse of equation 6, until all the absorbed energy is accounted for: we know this is a crude approximation [12]. The fraction α of incident energy that is absorbed is also needed.

Experimentation

Material property determinations. As stated in the introduction, the polymer studied was nylon-12, Duraform material from DTM. The stainless steel composition was (in weight %) 24Cr, 20Ni, 1.4Si, 0.9Mn, 0.44C, 0.006S, balance Fe. The solid polymer's specific heat, latent heat and melting temperature were found by differential scanning calorimetry (DSC). The metal's specific heat was found from hand-book data, its latent heat was estimated from its composition and its T_s and T_l temperatures from [13]. Thermal conductivity has been studied as a function of porosity in two ways, in the temperature range 20°C to ≈ 100°C: firstly by measuring the steady state temperature changes along an insulated cylindrical pile of a sample and comparator, heated at one end; and secondly (more recently) by the transient temperature response, at different depths below the powder bed surface, to a single line scan of a laser beam over the surface, of known power and speed. The first method has been used for the nylon powder and partially densified parts; and for the metal powder. The second method has been used for the metal powder; and has also enabled the metal powder bed absorbtivity α to be measured.

To estimate sintering behaviour of nylon-12, its viscosity was measured over the range of temperature 200°C to 240°C, at a strain rate of $1000s^{-1}$: the strain rate is higher than occurs in SLS but was what was possible with the equipment used. Surface tension and powder size data were obtained as described in the last section (sintering law for crystalline polymers).

Sintering experiments. Rectangular blocks (nominally 15 mm in the x direction (figure 1), 50 mm in y and 10 mm deep) and cylinders (diameter 70 mm, thickness 3mm and 6mm) were sintered from nylon-12 in DTM's Sinterstation 2000. Scan speed and spacing were constant at 1257 mm/s and 0.15mm (layer thickness was 0.1mm, beam diameter 0.4mm); laser power was from 1.6 to 5.4W. Scaling factors were set, from measurements to establish shrinkage allowance, at 1.035 (x), 1.044 (y) and 1.015 (z). Beam offset was set at 0.288mm (x) and 0.210mm (y), to give zero x- and y-dimensional errors at a power of 3.9W. Bed temperature was set at 182°C. Metal sintering was carried out in a research SLS machine with a room temperature powder bed and laser power of up to 250W and a controlled argon atmosphere [14]. Results are reported of single track tests, at a laser power of 100W and scan speeds from 0.5mm/s to 40 mm/s.

Simulations. Simulations are reported, with the input variables described above, and varying (for nylon-12) β, A_s (equation 3) and a_p (equation 6) and (for stainless steel) a_p and α (absorption coefficient), to improve the accuracy and test the sensitivity of the simulations to these variables.

Results

Material properties. Table 1 lists the measured and handbook material thermal properties used in the simulations; and Table 2 lists other data, to do with sintering laws, absorbtivity and density: the As and Es/R values for nylon-12 are calculated from equation 4. Table 2 includes data on the polycarbonate powder [9], used as a standard for determining the viscous sintering behaviour of the nylon-12 melt. The T_m and densities for nylon-12 differ slightly from published DTM data.
Table 1. Material thermal property data.

Material	L (kJ/kg)	T_m (°C)	T_s (°C)	T_l (°C)	$K_{s,o}$ (W/mK)	$a_{K,S}$ (W/mK^2)	$C_{p,o`}$ (J/kg)	a_c (J/kgK)	a_K (¾)
Nylon-12	108	186	n/a	n/a	0.26	0*	460**	7.8**	1.1
Stainless steel	308	n/a	1280	1380	7.83	0.0183	437	0.275	51.9

*: nylon-12 variation of conductivity with temperature ignored; **: for $T > T_m$

Table 2. Other material property data.

Material	r (μm)	A_η (Pa s)	E_η/R (K)	A_σ (N/m)	E_σ/R (K)	A_s (s^{-1})	E_s/R (K)	α (¾)	ρ_{solid} (kg/m^3)	ρ_{powder} (kg/m^3)
Polycarbonate	30*	$5.63x10^{-10}$	15148	0.020	217	$8.84x10^{16}$	21000	0.95	n/a	n/a
Nylon-12	58*	$2.01x10^{-4}$	6341	0.017	191	$1.1x10^{11}$	12220	0.95**	970	430
Stainless steel	≈150	n/a	n/a	n/a	n/a	n/a	n/a	0.21	7850	4710

*: mean values from [9] and commercial data sheets; **: assumed as for polycarbonate

Sintering tests and simulations for nylon-12. Figure 2a shows (·) the experimental variation of part density with laser energy density P/(Us). It is compared with three sets of predictions. In the first (¾), β is varied from 6 to 20 (β < 6 gives sintering at $T < T_m$), with $A_s = 1.1x10^{11}s^{-1}$ and $a_p = 0.01$: the last represents $\Delta z_p \approx$ zero. β = 10 is the base for the second set (- - -) in which Δz_p is varied up to 0.5mm. Finally ( ), A_s is increased up to $5x10^{11}s^{-1}$, for β = 10 and Δz_p = 0.25mm. Prediction matches experiments when $A_s \approx 2.5\ x10^{11}$ to $5x10^{11}s^{-1}$. It is only by setting $\Delta z_p > 0$ that the rapid change of part density with energy density between 0.01 and 0.02 J/mm^2 is predicted; and only by increasing A_s to $> 1.1x10^{11}s^{-1}$ that good high density prediction is found. Figure 2b compares experiments for y-(·) and z-(o) errors with predictions, for β = 10, Δz_p = 0.25mm and A_s = 2.5 to $5x10^{11}s^{-1}$. An issue is what density constitutes the edge of a part: 500 kg/m^3 and 450 kg/m^3 are tested. Reasonable agreement with experiment is found for simulations with $A_s = 5x10^{11}s^{-1}$ and edge density supposed to be 450 kg/m^3.

Sintering tests and simulations for stainless steel. Figure 3a shows the results of simulations of what absorbed laser power P and scan speed U combinations just cause a single track of stainless steel to melt. There are three sets of results, each for an assumed penetration depth Δz_p of laser energy into the powder bed. Also included is the experimental observation of what transmitted power-speed combinations actually cause the steel to melt, from [14]. The ratio of simulated to experimental P at a given U gives a prediction of the absorptivity α. The different values for each Δz_p are listed in the Figure. Figure 1b compares experimental and predicted single track widths and depths, for three sets of predictions depending on the three sets of Δz_p and α from Figure 1a. The width measurements agree with simulations, for the range of α between 0.26 and 0.41. This compares with a measured α of 0.21 (Table 2). The observed track depths, however, are greater than predicted. Experiments were carried out at speeds up to 40 mm/s, but above 12 mm/s, the tracks were too fragile to be lifted from the bed and measured.

Discussion and Conclusion

A good agreement between experiments on and simulation of the SLS of a crystalline polymer, nylon-12, has been obtained, but it has required three developments from the previous stage of simulating an amorphous polymer. Firstly a factor to reduce sintering rate as the degree of crystallinity increases has been included in the sintering law for the material: equation 3 has been found to be satisfactory for this. Secondly, a way of estimating the sintering rate in the molten state, from polymer melt viscosity tests and particle size, has been developed: equation 4 has been found to deliver the right order of magnitude for A_s and E_s/R, but a 5-fold correction to A_s has been required to obtain good agreement with experiment. The weakest part of equation 4 is describing powder size by a single radius r, when the particles are not spherical and have wide

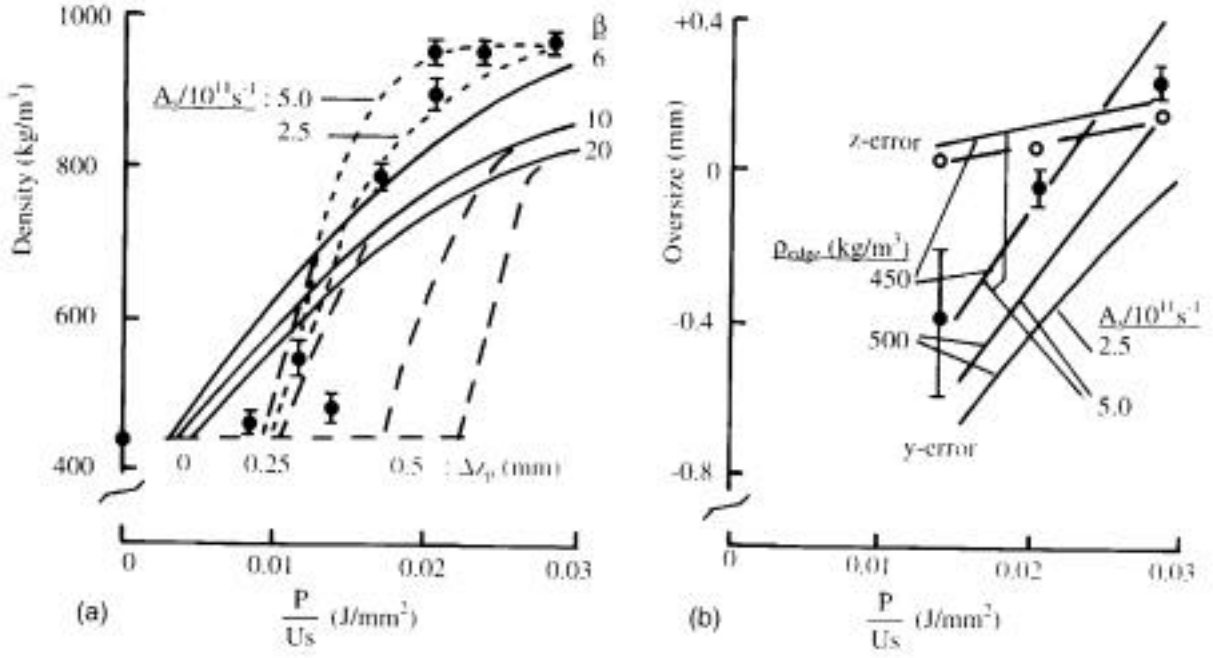

Figure 2. Experimental (· , o) and theoretical (¾, -.-., …) comparisons of (a) density and (b) y- and z-oversize dependence on energy density, for a nylon-12

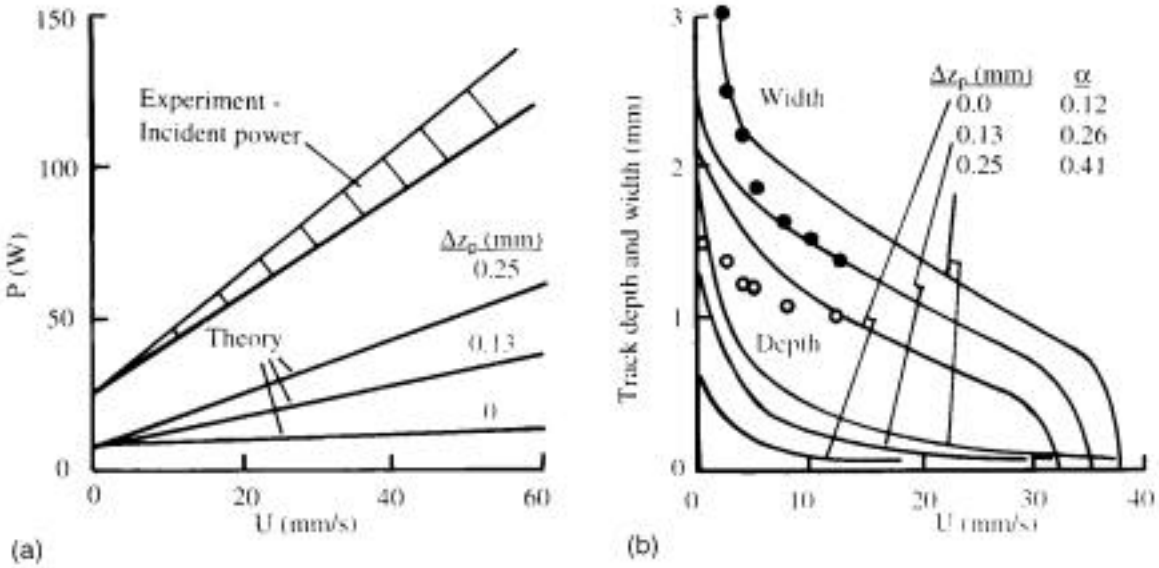

Figure 3. (a) experimental incident laser power and simulated absorbed power / scan speed relations to give initial sintering; (b) experimental (· , o) and predicted (¾) track widths and depths, for SLS of a stainless steel.

size distributions: perhaps refinements of this would yield more accurate predictions. Finally, an essential part of the simulation is to suppose the laser power to be absorbed over a finite depth of the powder bed. In the present case, a depth of 0.25 mm gave good agreement with experiments: this is about the depth Δh (Figure 1b) of a powder layer spread over a previously sintered layer. It is tempting to speculate that the layer thickness in SLS should be chosen so that, for a given size and packing of powder, the laser power penetration depth equals the layer thickness.

A three-dimensional simulation has been developed for direct metals SLS. Again, depth of absorption of the laser beam into the powder bed is important. Good agreement has been seen between measured and predicted single track width; but track depths are greater than predicted. Maybe the molten metal in a track drips under gravity, weakly to bond powder material to the body of the track: certainly the underside of a track looks powder-like: more work is required to resolve this. The simulation is now being applied to multi-tracks in a single layer and to multi-layer SLS. Laser powers to re-melt a previous layer under a current track are being estimated, but there is no space to report this work.

References

1. E. M. Weissman and M. B. Hsu (1991) A finite element model of multi-layered laser sintered parts. *Proc. 2nd Solid Freeform Fabrication Symposium*, University of Texas, Austin, pp.86-94.
2. J. C. Nelson (1993) *Doctoral Dissertation*, Austin: The University of Texas at Austin.
3. T. H. C. Childs, M. Berzins, G. R. Ryder and A. E. Tontowi (1999) Selective laser sintering of an amorphous polymer - simulations and experiments. *Proc. I.Mech.E. (Lond.)* **213B**, 333-49.
4. G. Bugeda, M. Cervera, and G. Lombera (1999) Numerical prediction of temperature and density distribution in selective laser sintering process. *Rapid Prototyping Journal* **5**, 21-26.

5. T. C. Tszeng, Y. T. Im and S. Kobayashi (1989) Thermal analysis of solidification by the temperature recovery method. *Int. J. Mach. Tools Manufact.* **29**, 107-20.
6. M. Shiomi, A. Yoshidome, F. Abe and K. Osakada (1999) Finite element analysis of melting and solidifying processes in laser rapid prototyping of metallic powders. *Int. J. Mach. Tools Manufact.* **39**, 237-52.
7. A. Ziabicki, L. Jarecki and A. Wasiak (1998) Dynamic modelling of melt spinning. *Computational and Theoretical Polymer Science* **8**, 143-57.
8. J. Frenkel (1945) Viscous flow of crystalline bodies under the action of surface tension. *J. Phys (USSR)* **9**, 385-91.
9. J. C. Nelson et al. (1993) Model of the selective laser sintering of bisphenol-A polycarbonate. *Ind. Eng. Chem. Res.* **32**, 2305-17.
10. J. Brandrup and E. H. Immergut (1989) *Polymer Handbook, 3rd edn.* London: John Wiley.
11. M. C. Flemings (1991) Behavior of metal alloys in the semi-solid state. *Metallurgical Transactions,* **22B**, 269-93.
12. X. Wang and J-P. Kruth (2000) Simulations of the selective laser sintering process. *Proc. 5th Belgian Nat. Congress on Theoretical and Applied Mechanics May 2000,* Louvain, pp. 39-42
13. Anon (1977) *A guide to the solidification of steels.* Stockholm: Jernkontoret.
14. C. Hauser, T. H. C. Childs, K. W. Dalgarno and R. B. Eane (1999) Atmospheric control during selective laser sintering of stainless steel 314S powder. In: *Proc. 10th Solid Freeform Fabrication Symposium,* University of Texas, Austin, pp.265-72.